TU Delft

Delft University of Technology

Document Version
Final published version

Licence
Dutch Copyright Act (Article 25fa)

Citation (APA)
Yupa Villanueva, R. M., Merino Martinez, R., Morin, A. M., & Snellen, M. (2026). Sound Quality Directivity Characterization of a Hovering Drone Using Microphone Array Measurements. In *32nd AIAA/CEAS Aeroacoustics Conference (2026)* Article AIAA 2026-3462 https://doi.org/10.2514/6.2026-3462

Important note
To cite this publication, please use the final published version (if applicable).
Please check the document version above.

Copyright
In case the licence states “Dutch Copyright Act (Article 25fa)”, this publication was made available Green Open Access via the TU Delft Institutional Repository pursuant to Dutch Copyright Act (Article 25fa, the Taverne amendment). This provision does not affect copyright ownership.
Unless copyright is transferred by contract or statute, it remains with the copyright holder.

Sharing and reuse
Other than for strictly personal use, it is not permitted to download, forward or distribute the text or part of it, without the consent of the author(s) and/or copyright holder(s), unless the work is under an open content license such as Creative Commons.

Takedown policy
Please contact us and provide details if you believe this document breaches copyrights.
We will remove access to the work immediately and investigate your claim.

This work is downloaded from Delft University of Technology.

Aeroacoustics Conferences
26-29 May 2026, Brussels, Belgium
32nd AIAA/CEAS Aeroacoustics Conference (2026)

10.2514/6.2026-3462

Check for updates

Sound Quality Directivity Characterization of a Hovering Drone using Microphone Array Measurements

Renatto M. Yupa-Villanueva *, Roberto Merino-Martínez †, Amy Morin ‡, and Mirjam Snellen §
Delft University of Technology, Kluyverweg 1, 2629 HS Delft, the Netherlands

Unmanned aerial vehicles are increasingly considered for urban operations, yet their noise emissions remain a key limitation due to their directional and perceptually complex character. This paper presents a three-dimensional acoustic and psychoacoustic characterization of a quadcopter drone measured under controlled free-field conditions in an anechoic chamber. A 112-channel phased microphone array was used to record the drone sound radiation for 19 azimuth angles and 11 vertical positions (polar angles). The overall sound pressure level (OSPL) and its A-weighted counterpart (OASPL) were employed to quantify the acoustic directivity and conventional frequency-domain beamforming was used to generate two-dimensional source maps at selected one-third-octave bands. Moreover, sound quality metrics, together with a psychoacoustic annoyance model, were evaluated to examine the directional dependence of perceived sound quality. The results show that energy-based metrics exhibit a dipole-like directivity pattern, characterized by a quasi-axisymmetric bi-lobed dependence with respect to the polar angles. The lowest and most nearly-isotropic radiation occurs close to the rotor plane (i.e., polar angles close to zero), and higher levels occurring as the polar angle is steered away from the drone's horizontal plane. The beamforming source maps reveal compact sources associated with the rotors at higher frequencies. Regarding perception, loudness and psychoacoustic annoyance broadly follow the OSPL and OASPL trends. In contrast, sharpness shows a more diffuse angular dependence. Tonality, roughness, and fluctuation strength show localized maxima, indicating that the loudest directions are not necessarily the most perceptually salient or annoying. Furthermore, the perceptual minima do not coincide with the minimum OSPL and OASPL directions. These findings confirm that purely energy-based metrics are insufficient to fully characterize the perceived nature of drone noise and contribute to a more complete characterization of drone noise for source identification, auralization, and mitigation-oriented design.

Downloaded by Technische Universiteit Delft on June 5, 2026 | http://arc.aiaa.org | DOI: 10.2514/6.2026-3462

I. Introduction

UNMANNED aerial vehicles (UAVs), widely referred to as drones, have rapidly gained popularity due to their diverse advantages in both commercial and recreational applications, including point-to-point delivery, photography, and various monitoring tasks [1]. Despite the inherent benefits offered by these vehicles, the noise pollution they generate represents a major obstacle that must be addressed before they can be widely incorporated into urban scenarios [2].

Acoustic measurements of drones can be performed in the field or under controlled conditions, such as anechoic laboratories. Field measurements enable the evaluation of realistic flight conditions [3]; however, they must account for uncontrollable factors, such as weather conditions or wind gusts [4]. On the other hand, measurements conducted in laboratories typically provide more controlled conditions and a higher

*PhD candidate, Operations & Environment section, Faculty of Aerospace Engineering, R.M.YupaVillanueva@tudelft.nl
†Assistant professor, Operations & Environment section, Faculty of Aerospace Engineering, R.MerinoMartinez@tudelft.nl
‡Research engineer, Operations & Environment section, Faculty of Aerospace Engineering, A.M.Morin@tudelft.nl
§Full professor, Operations & Environment section, Faculty of Aerospace Engineering, M.Snellen@tudelft.nl

Copyright © 2026 by the American Institute of Aeronautics and Astronautics, Inc. All rights reserved.

repeatability [5], but are limited in representing measurements for the full flight envelope. In particular, anechoic chambers offer the advantage of low background noise levels and (almost) free-field acoustic conditions that are useful for characterizing the acoustic source. Once the source is well characterized, the measured signals can be analytically manipulated, e.g., within auralization frameworks, to study the influence of different propagation effects or flight maneuvers on the sound perceived by a given observer [6, 7].

Given these advantages, anechoic chambers provide an ideal environment for elucidating drone noise directivity, especially when considering a three-dimensional approach. Drone noise emissions are known to be highly directional and non-uniform due to complex rotor–rotor and rotor–fuselage aerodynamic and acoustic interactions. Therefore, capturing their radiation patterns in all spatial directions is essential to understand how sound emissions vary across polar and azimuth angles. Additionally, evaluating the source not only with conventional acoustic metrics but also through perception-based metrics provides complementary insights into how these directional features are perceived by humans. A comprehensive three-dimensional characterization, therefore, enables a more complete description of the acoustic signature of drones and forms the foundation for accurate auralization, noise-prediction models, and the design of future mitigation strategies.

Therefore, the objectives of this research work are described below:

- To characterize the three-dimensional acoustic directivity of a commercial quadcopter drone under controlled anechoic conditions, in terms of overall sound pressure level (OSPL) and its A-weighted counterpart (OASPL) as a function of polar and azimuth angles.
- To identify the dominant sound-radiating regions of the drone and assess their frequency dependence by means of two-dimensional conventional frequency-domain beamforming at representative one-third-octave bands and observer positions.
- To evaluate the directional behavior of perception-based sound metrics, namely loudness, sharpness, tonality, roughness, fluctuation strength, and psychoacoustic annoyance, in order to determine how perceptual directivity complements and extends the information provided by OSPL alone.

II. Methodology

A. Experimental Setup

1. Drone

The quadcopter drone used in the experimental campaign was a *DJI Mavic 3 Enterprise*. Figure 1 shows the configuration and main dimensions of the drone. The drone was equipped with four two-bladed propellers with a diameter of 239 mm, thread pitch of 135 mm, and a weight of 8.5 g (per blade). The front and aft propellers are positioned at slightly different horizontal planes, as shown in Fig. 1b. The parameters to characterize the dimensions of the drone are shown in Fig. 1b (lateral view) and Fig. 1c (top view), where $H = 107.7$ mm indicates the height, $B = 347.5$ mm the width, and $L = 283$ mm the length.



(a) Perspective view of the drone and the two-bladed low-noise propeller.

(b) Lateral view.

(c) Top view.

Fig. 1 Dimensions of the *DJI Mavic 3 Enterprise* quadcopter drone.

2. Anechoic chamber

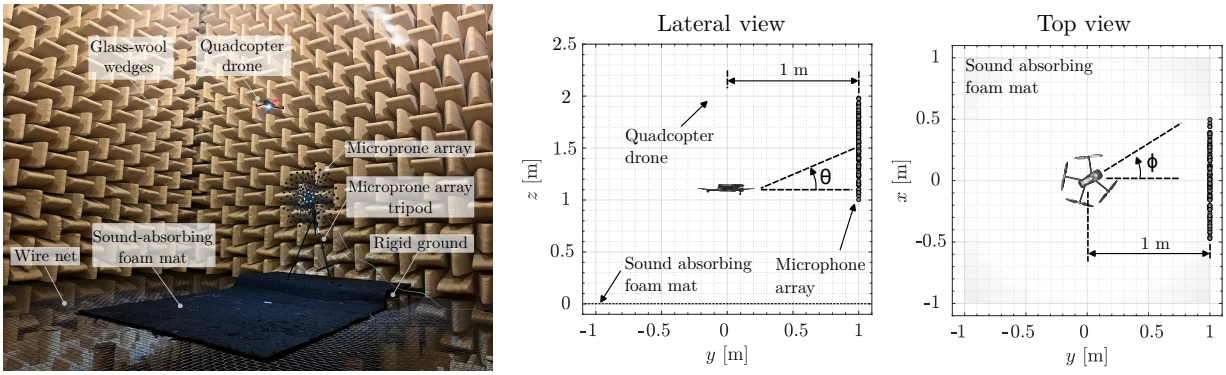
The experimental campaign was conducted in the anechoic chamber of the Faculty of Applied Science at Delft University of Technology. The chamber is an 8 m×8 m×8 m cube, with its walls, floor, and ceiling

Downloaded by Technische Universiteit Delft on June 5, 2026 | http://arc.aiaa.org | DOI: 10.2514/6.2026-3462

fully lined with 1-m-long glass-wool wedges, as shown in Fig. 2a. This treatment ensures free-field acoustic conditions for frequencies above 100 Hz. The room is completely isolated from the building structure and mounted on its own support system. This configuration allows a space free from mechanical vibrations with negligible background noise (approximately 5.5 dBA). Additionally, the chamber does not have a rigid floor; instead, a wire net is installed on which a rigid floor can be placed to support diverse equipment, such as the support tripod for the microphone array seen in Fig. 2a. To enable the drone to take off and land*, a sound-absorbing and thermally insulating polyester-wool mat (AKOTHERM D40/25) was placed over the wire net during the measurements. The mat has a density of 40 kg/m^3 and a thickness of 25 mm. In addition to supporting the operation of the drone, this mat reduces residual acoustic reflections more effectively than using only a rigid floor.

3. Phased microphone array

A *CAE Systems Bionic M-112* [8] phased microphone array was used to record the sound emissions generated by the drone. The array has a diameter of 1 m and consists of 112 digital MEMS microphones, as shown in Fig. 2a. The array was placed 1 m away from the center of the drone, as depicted in Fig. 2b. To perform three-dimensional measurements and obtain the directivity, the array was kept at a fixed position while the drone position was varied. To obtain multiple azimuth angles (ϕ), the drone was rotated around its vertical axis in increments of 10°, from 0° to 180°, resulting in nineteen azimuth positions. The azimuth angles $\phi = 0°$, 90°, and 180° represent the front, lateral, and rear sides of the drone relative to the array, respectively. The polar angles (θ) were obtained by varying the altitude of the drone relative to the array center, resulting in eleven discrete measurement positions spanning approximately $-50°$ to 50°. Positive values of θ indicate that the drone is located below the microphone array, and vice versa. Therefore, for each drone position, nineteen azimuth angles were considered, and for each azimuth angle, 112 acoustic signals were recorded, resulting in a total of 23408 acoustic signals from 209 measurement runs. In Fig. 2b, the definitions of θ and ϕ are presented. Each recording had a duration of 20 s.



(a) Picture of the experimental setup. **(b) Relative position of the drone and array.**

Fig. 2 Experimental setup within the anechoic chamber of the Faculty of Applied Physics of Delft University of Technology.

B. Acoustic and Psychoacoustic Metrics

Acoustic metrics are typically defined based on the acoustic energy received at a given location. In this work, the overall sound pressure level (OSPL) is adopted, providing an integrated measure of the acoustic energy over a specified frequency range. Acoustic directivity is commonly evaluated at a constant distance from the source to isolate angular radiation effects from propagation. In the present measurements, however, the distance between the drone and each microphone varies with position. As a result, the raw sound pressure levels inherently include geometric attenuation effects due to spherical spreading. To isolate the directivity of the source, all acoustic pressure signals were normalized to a common reference distance of 1 m using a spherical spreading correction, as expressed in Eq. 1. In this equation, k denotes the microphone index, $d_{\mathrm{mic},k}$ is the distance between the drone and the $k-$th microphone, and $d_{\mathrm{ref}} = 1$ m is the reference distance.

*Without such a mat, the drone flight control sensors did not allow a safe take-off.

Downloaded by Technische Universiteit Delft on June 5, 2026 | http://arc.aiaa.org | DOI: 10.2514/6.2026-3462

The parameters $p_{k,\mathrm{raw}}(t)$ and $p_{k,\mathrm{corrected}}(t)$ denote the raw and distance-corrected acoustic pressure signals measured at the $k-$th microphone, respectively. From the corrected signals, the sound pressure levels $L_p(f)$ were obtained for each microphone, defined as $L_p(f) = 20\log_{10}(p_{\mathrm{rms}}/p_{\mathrm{ref}})$, where $p_{\mathrm{ref}} = 20$ μPa. The OSPL was then computed for each microphone over the frequency range from 20 Hz to 20 kHz. In addition, the A-weighted overall sound pressure level (OASPL) was evaluated. This metric was obtained by applying the A-weighting filter to the corrected acoustic pressure signals prior to the OSPL computation. From this point onward, the same procedures used to describe the acoustic directivity are also applied to the OASPL. For simplicity, however, the equations are presented only in terms of OSPL.

$$p_{k,\mathrm{corrected}}(t) = p_{k,\mathrm{raw}}(t)\,\frac{d_{\mathrm{mic},k}}{d_{\mathrm{ref}}} \tag{1}$$

The acoustic directivity is first characterized using the individual microphone measurements (microphone-resolved directivity), preserving the angular resolution provided by the array. After obtaining the spherically-corrected OSPL per microphone, each microphone is then assigned angular coordinates relative to the instantaneous drone position. The polar angle θ_{k} and azimuth angle ϕ_{k} of the k-th microphone are defined in Eqs. 2 and 3, respectively, where (x_{k}, y_{k}, z_{k}) denote the microphone coordinates, (x_{d}, y_{d}, z_{d}) the drone position, and r_{k} the distance between the drone and the k-th microphone. For the analyzed cases, the drone position is defined as (x_{d}, y_{d})=(0, 0) m and y_{k} =1 m, as shown in Fig. 2b. Additionally, to account for the imposed azimuthal rotation of the drone between consecutive measurement runs, an effective azimuth angle is defined, as shown in Eq. 4, where ϕ_{rot} is the nominal rotation angle of the drone for each run.

$$\theta_k = \sin^{-1}\left(\frac{z_{\mathrm{k}} - z_{\mathrm{d}}}{r_{\mathrm{k}}}\right) \tag{2}$$

$$\phi_k = \tan^{-1}\left(\frac{x_{\mathrm{k}} - x_{\mathrm{d}}}{y_{\mathrm{k}} - y_{\mathrm{d}}}\right) \tag{3}$$

$$\phi_{k,\mathrm{eff}} = \phi_{\mathrm{k}} + \phi_{\mathrm{rot}} \tag{4}$$

A second representation of the acoustic directivity is based on the nominal drone orientation. In this approach, each measurement run is associated with a single angular position (θ, ϕ), defined by the imposed drone height and azimuthal rotation. A representative OSPL value is then obtained by performing an energetic average across all microphones, as shown in Eq. 5, where N is the total number of microphones. It should be noted that the application of the energetic average reduces the angular resolution by collapsing the microphone-resolved information into a single value per orientation. Therefore, this map is interpreted as a nominal-orientation directivity, complementary to the microphone-resolved analysis.

$$\mathrm{OSPL}(\theta,\phi) = 10\log_{10}\left(\frac{1}{N}\sum_{k=1}^{N} 10^{\mathrm{OSPL}_k/10}\right). \tag{5}$$

The psychoacoustic metrics are categorized into two groups: i) sound quality metrics (SQMs) and ii) psychoacoustic annoyance (PA) model. The SQMs describe the subjective perception of sound by human hearing, unlike the sound pressure level, which quantifies the purely physical magnitude of sound based on pressure fluctuations. Previous studies [9, 10] showed that these metrics better capture the auditory behavior of the human ear compared to conventional sound metrics typically employed in noise evaluations. The five most commonly used SQMs [11] are:

- Loudness: Subjective perception of sound magnitude of the overall sound intensity [12]. The unit of this metric is sone and it is expressed as $N_{\mathrm{ISO532-1:201}}$.
- Tonality: Measurement of the perceived strength of unmasked tonal energy within a complex sound [13]. The unit of this metric is t.u. and it is expressed as K_{Aures}.
- Sharpness: Representation of the high-frequency sound content [14]. The unit of this metric is acum and it is expressed as $S_{\mathrm{von\ Bismark}}$.
- Roughness: Hearing sensation caused by sounds with modulation frequencies between 15 Hz and 300 Hz [15]. The unit of this metric is asper and it is expressed as $R_{\mathrm{Daniel\,\&\,Weber}}$.
- Fluctuation strength: Assessment of slow fluctuations in loudness with modulation frequencies up to 20 Hz, with maximum sensitivity for modulation frequencies around 4 Hz [16]. The unit of this metric is vacil and it is expressed as FS_{Osses}.

The SQMs are expressed using the 5%-exceeded value (i.e., the 95$^{\mathrm{th}}$ percentile) obtained from a representative microphone located between the inner and outer diameters of the array for each measurement.

Downloaded by Technische Universiteit Delft on June 5, 2026 | http://arc.aiaa.org | DOI: 10.2514/6.2026-3462

This representative value is selected based on common practice in the literature, where the 95$^{\text{th}}$ percentile is often used to describe sound quality metrics, following the recommendation originally proposed for loudness by Fastl and Zwicker [17]. The PA model proposed by Di et al. [18] is used in this work, which combines the 95$^{\text{th}}$ percentile values of the SQMs into a single global metric. The expression for this PA model follows Eq. 6. The terms ω_S, ω_{FR}, and ω_T are weighting coefficients determined according to the adopted model and computed using Eqs. 7, 8, and 9, respectively.

$$PA = N\left(1 + \sqrt{w_S^2 + w_{FR}^2 + w_T^2}\right), \tag{6}$$

$$\omega_S = \begin{cases} 0.25(S - 1.75)\log_{10}(N + 10), & \text{for } S \geq 1.75 \\ 0, & \text{for } S < 1.75, \end{cases} \tag{7}$$

$$\omega_{FR} = \frac{2.18}{N^{0.4}}(0.4FS + 0.6R), \tag{8}$$

$$\omega_T = \frac{6.41}{N^{0.52}}K. \tag{9}$$

C. Conventional Frequency Domain Beamforming

Conventional Frequency Domain Beamforming (CFDBF) is one of the most widely used methods for acoustic source mapping due to its robustness, computational efficiency, and intuitive formulation [19]. This technique operates in the frequency domain and considers the recorded pressure signals from an array of N microphones as an N-dimensional complex vector $\boldsymbol{p}(f) \in \mathbb{C}^{N\times 1}$, which depends on the frequency f.

$$\boldsymbol{p}(f) = \begin{pmatrix} p_1(f) \\ \vdots \\ p_N(f) \end{pmatrix}. \tag{10}$$

Considering a single sound source located at the scan point $\boldsymbol{\xi}_j$, the received signal is modeled as $s_j\mathbf{g}_j$, where s_j denotes the source strength and $\mathbf{g}_j \in \mathbb{C}^{N\times 1}$ represents the so-called steering vector. The steering vector has N components, $\mathrm{g}_{j,n}$, with $n \in [1, \ldots, N]$, and represents the modeled acoustic transfer function between the pressure amplitudes at the mapped source location and at the microphone locations. Several steering vector formulations are available in the literature. For simplicity, omnidirectional, uncorrelated monopole sources are typically assumed, and differences between formulations arise mainly from the normalization of the steering vectors. For a stationary point source, the steering vector corresponds to the free-field Green's function associated with Helmholtz's equation.

$$\mathrm{g}_{j,n} = \frac{\exp\left(-2\pi i f\, \Delta t_{j,n}\right)}{4\pi\left|\mathbf{x}_n - \boldsymbol{\xi}_j\right|} = \frac{\exp\left(\frac{-2\pi i f\left|\mathbf{x}_n - \boldsymbol{\xi}_j\right|}{c}\right)}{4\pi\left|\mathbf{x}_n - \boldsymbol{\xi}_j\right|}, \tag{11}$$

where $|\cdot|$ denotes the Euclidean norm, $i^2 = -1$, and $\Delta t_{j,n}$ is the time delay between the emission and the reception of the signal by the observer. The vector $\mathbf{x}_n = (x_n, y_n, z_n) \in \mathbb{R}^{N\times 3}$, with $n = 1, \ldots, N$, represents the locations of the N microphones. An estimate of the source autopower, A, at a (potential) sound source located at the grid point $\boldsymbol{\xi}_j$ is obtained by minimizing, in a least-squares sense, the difference between the recorded pressure vector, $\boldsymbol{p}$, and the modeled pressure for a source at that grid point, $\boldsymbol{\xi}_j$, $s_j\mathbf{g}_j$. In Eq. 12, the operator $(\cdot)^*$ denotes the complex conjugate transpose of a vector, while $\langle\cdot\rangle$ represents the time average over several snapshots.

$$A(\boldsymbol{\xi}_j) = \frac{\mathbf{g}_j^*\left\langle \boldsymbol{p}\boldsymbol{p}^*\right\rangle \mathbf{g}_j}{\left|\mathbf{g}_j\right|^2}. \tag{12}$$

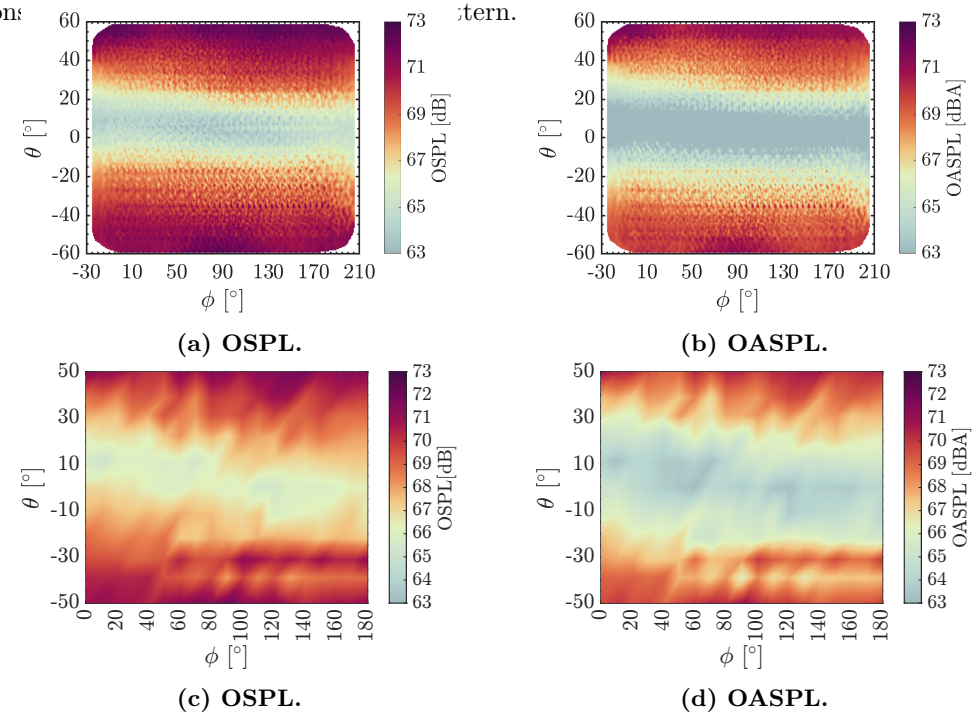
Downloaded by Technische Universiteit Delft on June 5, 2026 | http://arc.aiaa.org | DOI: 10.2514/6.2026-3462

III. Results

A. Acoustic Directivity

The OSPL and OASPL directivity patterns are shown in Fig. 3. The microphone-resolved representations shown in Figs. 3a–3b exhibit a consistent directivity behavior: sound levels are higher at large polar angles ($|\theta| > 20°$) and exhibit a pronounced low-level region around the mid-plane ($\theta \approx 0°$), extending roughly to $\pm 20°$ for all azimuths. This central region represents a local minimum in sound radiation rather than an absence of noise. The pattern exhibits little variation with azimuth angle, implying a quasi-axisymmetric radiation field. The OASPL distribution closely mirrors the OSPL pattern but with slightly lower magnitudes (due to A-weighting) and a marginally broader central low-level zone. The minimum and maximum OSPL values are observed at $(\theta, \phi) = (2°, 25°)$ and $(59°, 135°)$, respectively, while the corresponding OASPL values occur at $(3°, 63°)$ and $(52°, 5°)$. The two-lobed dependence on the polar angle (peaks at positive and negative θ) suggests a dipole-like radiation signature, which is typical for loading noise mechanisms in rotating machinery.

Figs. 3c–3d present the OSPL and OASPL levels based on the energetic-averaging approach. The overall trend remains similar to the microphone-resolved approach (comparable high-level lobes and a central trough), but the angular resolution is coarser, and some differences appear due to the averaging across the 112 microphones. Consequently, slight discrepancies are seen between the two methods, although the central low-level zone persists in both OSPL and OASPL. The minimum and maximum OSPL values are observed at $(\theta, \phi) = (0°, 10°)$ and $(\theta, \phi) = (50°, 130°)$, respectively, while the corresponding OASPL values occur at $(\theta, \phi) = (0°, 60°)$ and $(\theta, \phi) = (50°, 0°)$. To quantify these differences, the spatial standard deviation of OSPL and OASPL (Fig. 4) is computed, which shows the largest deviations for $|\theta| < 20°$ (reaching about 2.5 dB OSPL and 3 dBA OASPL at roughly $(\theta, \phi) = (60°, 20°)$. These deviation maps highlight where the microphone-resolved and averaged methods diverge. Importantly, the energetic-averaging approach reduces the angular extent of the results, since the values are referenced to the array's center, whereas the microphone-resolved pattern covers the full array aperture. Overall, the OSPL and OASPL directivity remains bi-lobed with respect to the polar angle: it is lowest and nearly isotropic at $\theta = 0°$, and it increases with $|\theta|$, cons tern.

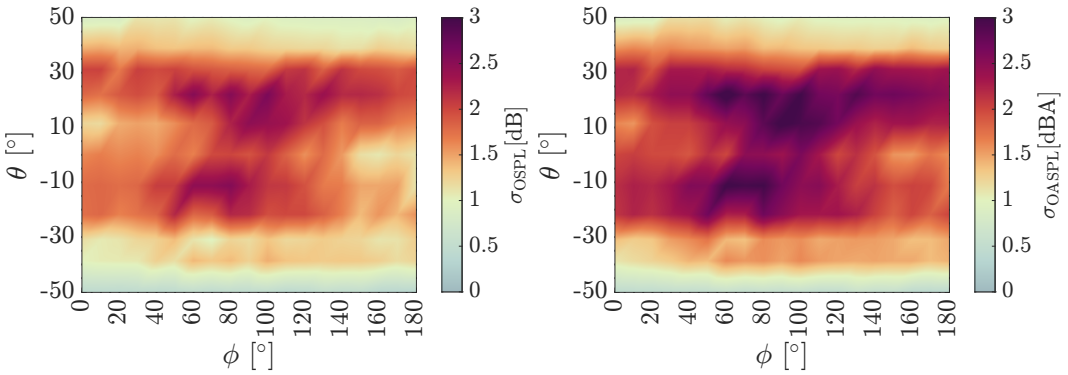


(a) OSPL. **(b) OASPL.**

(c) OSPL. **(d) OASPL.**

Fig. 3 OSPL and OASPL directivity maps. Figs. 3a-3b are computed using the microphone-resolved approach, while Figs. 3c-3d using the energetic average. The color scheme follows that proposed by Weninger [20], developed for the visualization of noise emission and immission.

Downloaded by Technische Universiteit Delft on June 5, 2026 | http://arc.aiaa.org | DOI: 10.2514/6.2026-3462



(a) σ_{OSPL}. **(b)** σ_{OASPL}.

Fig. 4 Heat maps of standard deviation of OSPL (σ_{OSPL}) and OASPL (σ_{OASPL}) directivity obtained from the energetic average.

Downloaded by Technische Universiteit Delft on June 5, 2026 | http://arc.aiaa.org | DOI: 10.2514/6.2026-3462

B. Two-dimensional Source Mapping

To complement the quantitative OSPL directivity, two-dimensional beamforming-based acoustic source maps are computed for four one-third-octave bands with central frequencies of 800, 1250, 2000, and 4000 Hz, for three drone positions (front, $\phi = 0°$; lateral, $\phi = 90°$; and back, $\phi = 180°$), all at $\theta = 0°$, as shown in Fig. 5. To ensure that the source maps are not influenced by scan grid discretization, the limited spatial resolution at the analyzed frequencies is first estimated using the Rayleigh resolution limit [21], given by the beamwidth (BW), where BW $\approx 1.22, ch/(Df)$[†]. Applying this expression yields spatial resolutions of 0.52 m at 800 Hz, 0.33 m at 1250 Hz, 0.21 m at 2000 Hz, and 0.10 m at 4000 Hz. Therefore, a scan grid discretization of 0.01 m is selected in both the y and z directions over a square plane ranging from -0.8 m to 0.8 m along each axis. Since the center of the drone is located at $y = 0$ m and aligned with the array center, the 2D scan grid is defined on this plane. Whereas OSPL describes how strongly the drone radiates sound energy as a function of direction, the acoustic images reveal which regions of the drone dominate the radiation at representative spectral components. For this purpose, a geometrical CAD model of the drone analyzed in this manuscript is also included within each source map. To analyze source location, spatial extent, and symmetry across different drone positions and frequencies, the L_{p} quantities obtained for each one-third-octave band are normalized as $(L_{\mathrm{p}} - L_{\mathrm{p,min}})/(L_{\mathrm{p,max}} - L_{\mathrm{p,min}})$. Although the source maps were normalized, a fixed dynamic range of 10 dB relative to the maximum level of each map was used for visualization purposes. Nevertheless, it is important to highlight that this normalization does not allow the assessment of the absolute source strength.

The source maps at 800 Hz are spatially broad and should not be interpreted as indicating a physically large source, but rather as a consequence of the limited array resolution at low frequencies. As the frequency increases to 1250 and 2000 Hz, the maps contract and exhibit more structured patterns. This trend is partly driven by the improved resolution, but is also qualitatively consistent with the drone noise characteristics, suggesting that strong acoustic sources may occur in the gaps between adjacent propellers, which can be interpreted as interaction noise between nearby rotors. In particular, at 2000 Hz, two dipole-like structures appear to merge, forming a four-lobed pattern in the front view ($\phi = 0°$). This map highlights the presence of four dominant sources associated with the rotors, which appear as two dipole-like structures due to the two-dimensional nature of the scan plane. For the lateral view ($\phi = 90°$) at 2000 Hz, the pattern becomes more compact and elongated in the vertical direction. Additionally, it can be observed that the two-lobed pattern appears to be tilted, which may be related to the fact that the front and rear rotors are located on different planes. When observing the back side of the drone ($\phi = 180°$), a similar four-lobed pattern emerges in the 2D scan plane, although it is less defined than in the front view. At 4000 Hz, the maps become even more compact, reflecting the improved localization associated with shorter wavelengths.

[†]In this equation, D represents the array aperture, f the frequency, c the speed of sound, and h the distance between the array and the sound source.

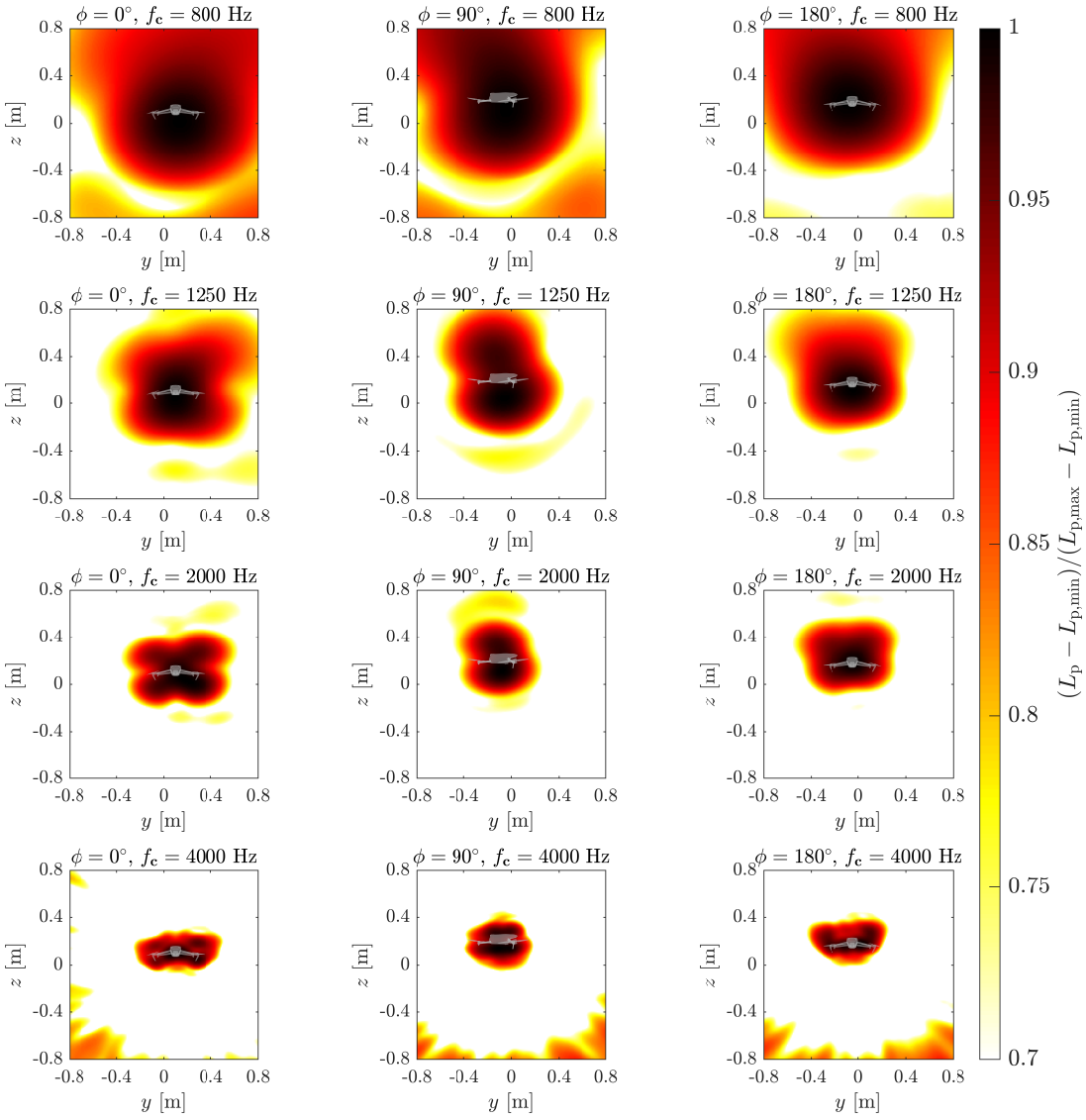


Fig. 5 Two-dimensional source mapping for the front (1st column), lateral (2nd column), and back (3rd column) sides of the drone facing the CAE array. Each row corresponds to 800, 1250, 2000, and 4000 Hz.

Downloaded by Technische Universiteit Delft on June 5, 2026 | http://arc.aiaa.org | DOI: 10.2514/6.2026-3462

C. Sound Quality Directivity

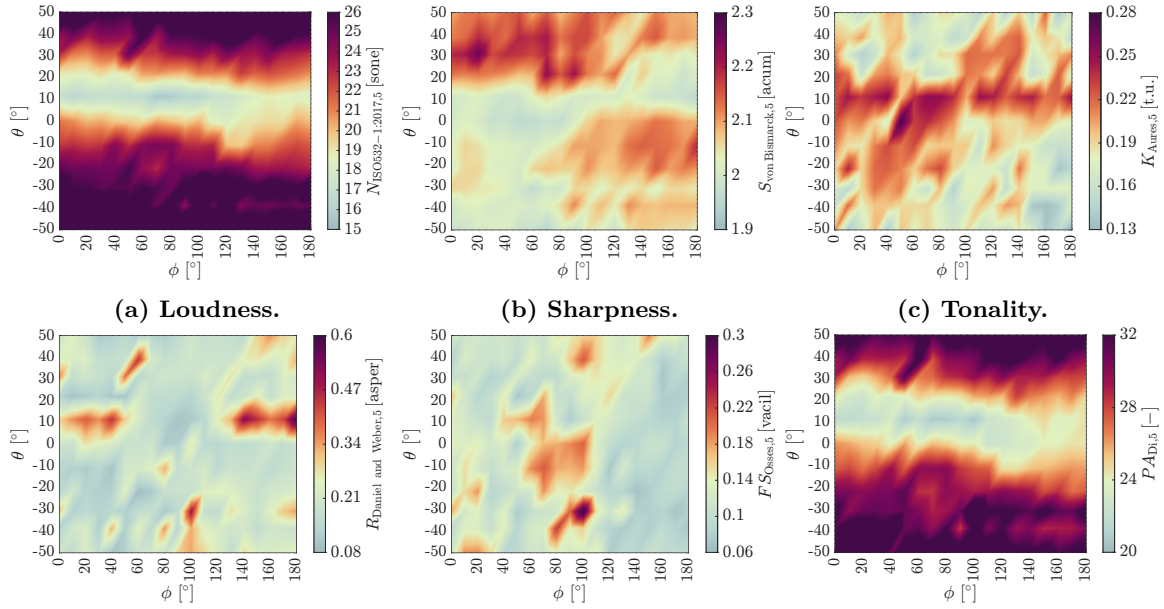
The sound quality directivity is presented in Fig. 6 for loudness, sharpness, tonality, roughness, fluctuation strength, and psychoacoustic annoyance. The contour maps fall into two broad families. Loudness and psychoacoustic annoyance exhibit the smoothest and closest behavior to the OSPL and OASPL directivities, with clear dependence on the polar angle and broad zones of high values. Sharpness shows weaker spatial variations, while tonality, roughness, and fluctuation strength are dominated by local maxima. In perceptual terms, Sec. III.A established the global directivity in terms of OSPL and OASPL, but the current results show that equal or near-equal radiated sound levels do not necessarily imply equal perceived character.

Among these metrics, loudness (Fig. 6a) and psychoacoustic annoyance (Fig. 6f) exhibit the most pronounced angular dependence. Similar to the OSPL and OASPL directivities, both quantities display a bi-lobed dependence on the polar angle, with lower values when the drone is located close to the array center ($\theta \approx 0°$) and substantially higher values for large $|\theta|$. However, the perceptual minimum is shifted toward

$\theta \approx 10°$: loudness reaches its lowest value at $\theta = 10°$ (17.19 sone), whereas the reference condition at $\theta = 0°$ yields 19.69 sone despite corresponding to the minimum OSPL and OASPL values. The highest loudness occurs at (θ, ϕ)=(-50°, 90°) with 30.82 sone. Psychoacoustic annoyance follows the same overall trend, but its maximum is observed at (θ, ϕ)=(-30°, 100°) with a value of 36.18, rather than at the loudest direction. This indicates that the most annoying direction is not determined by the loudness magnitude alone, but also by additional spectral and modulation-related penalties. Furthermore, the locations of the minimum and maximum values of loudness and psychoacoustic annoyance differ from those obtained in terms of OSPL and OASPL, which may be explained by the penalty contributions associated with the sound quality attributes.

Sharpness (Fig. 6b) shows a weaker directivity compared to loudness, ranging within the interval between 1.9 and 2.26 acum, with local maxima mainly at $0° \leq \phi \leq 180°$ for $\theta > 10°$ and at $70° \leq \phi \leq 180°$ for $\theta < 10°$. Tonality (Fig. 6c) exhibits a distinct angular dependence, reaching its maximum at (θ, ϕ) = (0°, 50°) with a value of 0.279 t.u., while its highest values concentrated around $\theta = 10°$ for all azimuth angles. By contrast, the region around $\theta = -50°$ is less tonal, with a mean value of 0.170 t.u. and the global minimum at $\phi = 180°$. Hence, the directions of highest emitted energy are not necessarily the directions of highest tonal salience. This is physically plausible because the Aures tonality metric depends on the prominence of tonal components relative to their masking background, i.e., when the blade-passing harmonics are most salient to a listener.

Roughness (Fig. 6d) and fluctuation strength (Fig. 6e) exhibit the most localized directivity patterns, with isolated local maxima instead of smooth lobes. The maximum roughness is obtained at (θ, ϕ) = (10°, 180°) with 0.598 asper, whereas the maximum fluctuation strength occurs at (θ, ϕ) = (−30°, 100°).



(a) Loudness. **(b) Sharpness.** **(c) Tonality.**

(d) Roughness. **(e) Fluctuation strength.** **(f) Psychoacoustic annoyance.**

Fig. 6 Three-dimensional sound quality directivity expressed as heat maps.

IV. Conclusions

This paper presented a controlled anechoic-chamber methodology for the three-dimensional characterization of drone noise by combining phased-array measurements, distance-corrected acoustic analysis, conventional frequency-domain beamforming, and psychoacoustic evaluation. Using a dense set of polar and azimuth angles, the study characterized the quadcopter drone not only in terms of radiated sound energy but also in terms of the spatial distribution of dominant source regions and the direction-dependent perceptual attributes of the emitted sound. In this way, the work provides a more complete description of the drone's acoustic signature and establishes a useful basis for future drone-noise prediction, auralization, and mitigation studies. The conclusions obtained from this investigation regarding the three objectives are presented below:

Downloaded by Technische Universiteit Delft on June 5, 2026 | http://arc.aiaa.org | DOI: 10.2514/6.2026-3462

- **Acoustic directivity**: The acoustic directivity exhibits a bi-lobed dependence on the polar angle, with minimum and nearly isotropic radiation around $\theta \approx 0°$ and increasing levels for larger $|\theta|$, consistent with a dipole-like pattern associated with rotor loading noise. This behavior is observed for both OSPL and OASPL, the latter showing slightly lower levels and a wider low-level region due to A-weighting. The weak azimuthal variation indicates a quasi-axisymmetric radiation field. While energetic averaging reduces angular resolution, it preserves the main features of the directivity. Standard deviation analysis shows that differences between both representations are mainly confined to $|\theta| < 20°$, reaching up to $\sim$2.5 dB (OSPL) and $\sim$3 dBA (OASPL). Overall, the drone radiates sound predominantly away from the rotor plane.

- **Source mapping**: The beamforming results indicate that the source distribution is strongly frequency-dependent. At low frequency, the mapped sources are spatially broad mainly because of the limited array resolution, while, at higher frequencies, the maps become progressively more compact and structured. In particular, the mid- and high-frequency maps reveal dominant source regions associated with the rotor system and suggest interaction-related radiation patterns between neighboring propellers and fuselage.
- **Perceptual directivity**: The psychoacoustic analysis shows that the directions of maximum emitted energy are not necessarily the directions of maximum annoyance. Loudness and psychoacoustic annoyance broadly follow the OSPL and OASPL trends. The minimum values of loudness and psychoacoustic annoyance are located around $\theta \approx 10°$, in contrast to the minimum OSPL and OASPL magnitudes observed around $\theta \approx 0°$, which may be explained by the penalty contributions associated with the sound quality attributes. Sharpness exhibits a weaker and more diffuse angular dependence, indicating limited sensitivity to spatial variations compared to loudness. Meanwhile, tonality, roughness, and fluctuation strength are dominated by localized maxima, demonstrating that perceptual attributes can vary significantly even when overall sound levels remain similar. These results confirm that energy-based metrics alone are insufficient to fully describe the perceived nature of drone noise.

Future work will include the analysis of other drone designs and maneuvers using a similar methodology and the asynchronous combination of the different microphone array measurements for volumetric acoustic source mapping [22].

V. Acknowledgments

This publication is part of the project *Listen to the future* (with project number 20247) of the research programme Veni 2022 (Domain Applied and Engineering Sciences) granted to Roberto Merino-Martinez, which is (partly) financed by the Dutch Research Council (NWO). The authors also acknowledge the funding received from the IMAFUSA (IMpact and capacity Assessment Framework for U-space Societal Acceptance) – SESAR 3 joint undertaking project (number 101114776). The authors would like to thank Henry den Bok, room administrator of the anechoic chamber of the Faculty of Applied Physics, for his support during the measurement campaign.

References

[1] Floreano, D., and Wood, R. J., "Science, technology and the future of small autonomous drones," *nature*, Vol. 521, No. 7553, 2015, pp. 460–466. https://doi.org/10.1038/nature14542.

[2] Schäffer, B., Pieren, R., Heutschi, K., Wunderli, J. M., and Becker, S., "Drone noise emission characteristics and noise effects on humans—a systematic review," *International journal of environmental research and public health*, Vol. 18, No. 11, 2021, p. 5940. https://doi.org/10.3390/ijerph18115940.

[3] Yupa-Villanueva, R. M., Merino-Martinez, R., Altena, A., and Snellen, M., "Psychoacoustic characterization of multirotor drones in realistic flyover maneuvers," *30th aiaa/ceas aeroacoustics conference (2024)*, 2024, p. 3015. https://doi.org/doi.org/10.2514/6.2024-3015.

[4] Lotinga, M. J., Ramos-Romero, C., Green, N., and Torija, A. J., "Noise from unconventional aircraft: a review of current measurement techniques, psychoacoustics, metrics and regulation," *Current Pollution Reports*, Vol. 9, No. 4, 2023, pp. 724–745. https://doi.org/doi.org/10.1007/s40726-023-00285-4.

[5] Naz, P., Hengy, S., Ramamonjy, A., Rassy, O., and Bavu, E., "Outdoor field trials for the measurement of the

Downloaded by Technische Universiteit Delft on June 5, 2026 | http://arc.aiaa.org | DOI: 10.2514/6.2026-3462

acoustic signals of mini UAVs," *e-Forum Acusticum 2020*, 2020, pp. 3155–3162. https://doi.org/10.48465/fa.2020.0224.

[6] Heutschi, K., Ott, B., Nussbaumer, T., and Wellig, P., "Synthesis of real world drone signals based on lab recordings," *Acta Acustica*, Vol. 4, No. 6, 2020, p. 24. https://doi.org/10.1051/aacus/2020023.

[7] Dreier, C., and Vorländer, M., "Drone auralization model with statistical synthesis of amplitude and frequency modulations," *Acta Acustica*, Vol. 8, 2024, p. 35. https://doi.org/10.1051/aacus/2024026.

[8] CAE Bionic M-112, "Acoustic Camera 112 Microphones," https://www.cae-systems.de/en/products/acoustic-camera-sound-source-localization/bionic-m-112.html, 2025. Last visited: 29 October 2025.

[9] Merino-Martinez, R., Pieren, R., and Schäffer, B., "Holistic approach to wind turbine noise: From blade trailing–edge modifications to annoyance estimation," *Renewable and Sustainable Energy Reviews*, Vol. 148, No. 111285, 2021, pp. 1–14. https://doi.org/10.1016/j.rser.2021.111285, URL https://doi.org/10.1016/j.rser.2021.111285.

[10] Merino-Martinez, R., Pieren, R., Schäffer, B., and Simons, D. G., "Psychoacoustic model for predicting wind turbine noise annoyance," 24^{th} *International Congress on Acoustics (ICA), October 24 – 28 2022, Gyeongju, South Korea*, 2022. URL https://www.researchgate.net/publication/364996997_Psychoacoustic_model_for_predicting_wind_turbine_noise_annoyance.

[11] Greco, G. F., Merino-Martinez, R., Osses, A., and Langer, S. C., "SQAT: a MATLAB-based toolbox for quantitative sound quality analysis," 52^{th} *International Congress and Exposition on Noise Control Engineering, August 20 – 23 2023, Chiba, Greater Tokyo, Japan*, International Institute of Noise Control Engineering (I-INCE), ???? URL https://www.researchgate.net/publication/373334884_SQAT_a_MATLAB-based_toolbox_for_quantitative_sound_quality_analysis.

[12] "ISO norm 532–1 – Acoustics – Method for calculating loudness – Zwicker method," Tech. Rep. 1, International Organization for Standardization, 2017. URL https://www.iso.org/obp/ui/#iso:std:iso:532:-1:ed-1:v2:en.

[13] Aures, W., "Procedure for calculating the sensory euphony of arbitrary sound signal. In German: Berechnungsverfahren für den sensorischen Wohlklang beliebiger Schallsignale," *Acustica*, Vol. 59, No. 2, 1985, pp. 130–141. URL https://www.ingentaconnect.com/contentone/dav/aaua/1985/00000059/00000002/art00008.

[14] von Bismark, G., "Sharpness as an attribute of the timbre of steady sounds," *Acta Acustica united with Acustica*, Vol. 30, No. 3, 1974, pp. 159–172. URL https://www.semanticscholar.org/paper/Sharpness-as-an-attribute-of-the-timbre-of-steady-Bismarck/9576a2a74bff46ee0cded25bfd9e4302b4fb0470.

[15] Daniel, P., and Webber, R., "Psychoacoustical Roughness: Implementation of an Optimized Model," *Accustica – acta acustica*, Vol. 83, 1997, pp. 113–123. URL https://www.ingentaconnect.com/contentone/dav/aaua/1997/00000083/00000001/art00020.

[16] Osses, A., García León, R., and Kohlrausch, A., "Modelling the sensation of fluctuation strength," 22^{nd} *International Congress on Acoustics (ICA), September 5 – 9 2016, Buenos Aires, Argentina*, 2016. URL https://pure.tue.nl/ws/portalfiles/portal/52366479/Osses_Garcia_Kohlrausch_ICA2016_ID113.pdf.

[17] Fastl, H., and Zwicker, E., *Psychoacoustics: Facts and Models*, 3^{rd} ed., Springer-Verlag, Berlin, Germany, 2007. https://doi.org/doi.org/10.1007/978-3-540-68888-4.

[18] Di, G.-Q., Chen, X.-W., Song, K., Zhou, B., and Pei, C.-M., "Improvement of Zwicker's psychoacoustic annoyance model aiming at tonal noises," *Applied Acoustics*, Vol. 105, 2016, pp. 164–170. https://doi.org/10.1016/j.apacoust.2015.12.006.

[19] Van Veen, B. D., and Buckley, K. M., "Beamforming: A versatile approach to spatial filtering," *IEEE assp magazine*, Vol. 5, No. 2, 1988, pp. 4–24. https://doi.org/10.1109/53.665.

[20] Weninger, B., "A color scheme for the presentation of sound immission in maps: requirements and principles for design," *Euro Noise*, Vol. 2015, 2015, pp. 439–444. URL https://api.semanticscholar.org/CorpusID:198117884.

[21] Lord Rayleigh, F. R. S., "XXXI. Investigations in Optics with special reference to the Spectroscope," *The London, Edinburgh and Dublin Philosophical Magazine and Journal of Science*, Vol. 8, No. 49, 1879, pp. 261–274. https://doi.org/10.1080/14786447908639684.

[22] Pereira, L. T. L., Merino-Martínez, R., Ragni, D., Gómez-Ariza, D., and Snellen, M., "Combining asynchronous microphone array measurements for enhanced acoustic imaging and volumetric source mapping," *Applied Acoustics*, Vol. 182, 2021, p. 108247. https://doi.org/10.1016/j.apacoust.2021.108247.

Downloaded by Technische Universiteit Delft on June 5, 2026 | http://arc.aiaa.org | DOI: 10.2514/6.2026-3462